AEM cross-gradient constrained inversion of gravity and magnetic data

Adrián M. León-Sánchez*
Applied Geophysics, CICESE
Ensenada-Tijuana 3918, Zona Playitas,
Baja California, 22860, México
aleon@cicese.edu.mx

Luis A. Gallardo
Applied Geophysics, CICESE
Ensenada-Tijuana 3918, Zona Playitas,
Baja California, 22860, México.
lgallard@cicese.mx

A. Yusen Ley-Cooper
Mineral Resources, CSIRO
Bentley, WA, 6102, Australia.
yusen.ley@csiro.au

SUMMARY

Nowadays magnetics, electromagnetics and gravity are among the most abundant airborne surveys. Traditionally they aim at specific depth targets. For instance, Airborne Electromagnetic (AEM) data are known to provide reliable models of a few hundred meters deep; whereas, gravity and magnetic data can reveal geological features below few thousand meters depth. This depth-resolution difference has historically limited the combined interpretation of these data. We, however, hypothesize that there is a commonly sensed depth interval, which could be used to harness the joint inversion of the data and increase the reliability of the models in the wider depth extent. To demonstrate this we designed three inversion experiments using potential and AEM field data acquired in Western Australia. Firstly, we inverted each data set separately using a conventional 2D inversion strategy. Secondly, we jointly inverted the gravity and magnetic data using the cross-gradient constraint. Thirdly, we added a preliminary AEM resistivity model as a cross-gradient constraint for the 2D cross-gradient joint inversion of the gravity and magnetic datasets. Our results show that the three data sets sense a common area of the subsurface and that the vertical resolution of each data set influences in the shallow and deep structures of the joint models.

Key words: Cross-gradient, joint inversion, AEM data, potential data, Western Australia.

INTRODUCTION

For decades, airborne geophysics has helped to cover large and inaccessible areas considered prominent for exploration and targeting at a minimum cost and with sufficient depth and spatial resolution (Reeves et al. 1997). Because airborne geophysics allows us to acquire several geophysical data types simultaneously, it seems natural to combine all the available information to generate a better and more accurate interpretation.

One technique that has the capability of combining several data types is the cross-gradient joint inversion (Gallardo and Meju, 2003). This methodology has shown excellent results with many different combinations of geophysical data types (Gallardo and Meju, 2004, 2007; Gallardo, 2007; Moorkamp et al., 2011; Doetsch et al., 2011; Gallardo et al., 2012); however, it has not, as yet, been applied to AEM data.

In order get better results, similar spatial resolution of the involved data sets is required when the cross-gradient methodology is applied. It is know that potential field models reach depths between 5 and 15 km; however, potential field data also carries information of shallow geological structures (less than 600 meters depth), which is the depth where AEM data are more sensible. Our hypothesis is that even when potential and AEM data sets have different spatial resolution, the larger potential field structures will help to resolve vertically and laterally the resistive structures. To probe this, we used gravity, magnetic and AEM data sets acquired in the Capricorn Orogen in Western Australia and developed three inversion experiments. Firstly, we inverted each data set separately. Secondly, we performed a 2D cross-gradient joint inversion of the gravity and magnetic datasets. Thirdly, we added an AEM resistivity model as a constraint for the 2D cross-gradient joint inversion of the gravity and magnetic datasets.

Our results (León-Sánchez *et al.*, manuscript submitted, 2016) show that there is an area commonly sensed by all the data sets. The shallower structures are greatly influenced by the AEM data; while, the deeper structures are mainly determined by the potential data. We make use of geospectral images (Gallardo, 2007) to present our results.

GRAVITY, MAGNETIC AND AEM DATA SETS

We developed all our experiments along a 10 km long segment of the regional AEM flight line number 1016701. This segment shows evident heterogeneity in electrical conductivity, gravity and magnetic responses. The location of the 10 km long segment is shown in Figure 1. The AEM data are part of the largest AEM survey flown in Western Australia up to date (146,300 km^2) and were acquired using a fixed-wing TEMPEST system (Lane et al., 2000). The field data for the AEM survey is shown in Figure 2d. The gravity and magnetic data sets were provided by the Geophysical Archive Data Delivery System (GADDS) from Geoscience Australia. Both data sets extend between the longitudes E115.5°-E118° and latitudes S22°-S26°, which cover almost half of the AEM line 1016701. For gravity, we used the Bouguer anomaly extracted directly from the data base. The magnetic data were reduced to the pole (RTP) to avoid transversal phase shifting in our 2D magnetic model. Both profiles are shown in Figure 2a.

JOINT INVERSION OF POTENTIAL AND AEM DATA SET

We divided the 10 km long segment into 50 meters-wide cells. The cell width of each side of the 10 km segment was increased exponentially until they reach 100 km beyond the profile end. To fulfil the 2D assumption, the transversal length of the cells was set to 100 km. Vertically, the cell thicknesses vary from 10 meters at the surface to 2 km at 5m depth. The initial model for each data set is completely homogeneous with null density and magnetization contrast and constant resistivity.

Conventional 2D inversion of potential and AEM data sets

For this experiment we used the unconstrained version of the algorithm of Gallardo (2007) and the gravity and magnetic profile data shown in Figure 2a. We tested several damping factors (ranging from 0.01 to 100) in order to find the smoothest model that fit adequately their corresponding data set. The resulting models for the gravity and magnetic data sets are shown in Figures 2b and 2c, respectively. From them, it is possible to detect certain structural similarity in three large regions clearly visible in both models and the field data themselves. These heterogeneities are evinced in the residual variations (Figure 2f) between the 4 km and 8 km positions of the profile (cf. Figure 2a).

To obtain the AEM conductivity model (Figure 2e) we used the Geoscience Australia's Layered Earth Inversion (GA-LEI) algorithm (Brodie, 2010) to invert the AEM field data shown in Figure 2d. Since this model results from the lateral stitching of layered models for each individual sounding, an hypothetical 1 mSm background resistivity appears after the sounding data lose resolution (magenta line in Figure 2e).

It is worth mentioning that the three regions shown in the density and magnetization models are not visible in the conductivity model and that shallow electrical layering does not reflect in the density and magnetization models.

2D cross-gradient joint inversion of gravity and magnetic data sets

For this second experiment we used the cross-gradient constraint algorithm developed by Gallardo (2007). The resulting models are shown in Figures 3a and 3b. In the resulting models, the structural correspondence imposed by the cross-gradient constraint is clearly noticeable and, in particular, that the algorithm recovers various structures at depth, which are needed to justify the short wavelength variations on the profile data. As in the late experiment, it became difficult to justify the data in the profile segment between 4 km and 8 km (Figure 3c); however, the structures outside this interval are better delineated than those of the previous experiment.

2D cross-gradient joint inversion of gravity and magnetic data sets constrained by the AEM resistivity model

In our third experiment, we followed the lithotype inversion strategy described in Gallardo and Meju (2011) and adopted it to incorporate the AEM electrical resistivity values of Figure 2e in the joint inversion. From Figure 2e we selected only the resistivity values above the magenta line, which is deemed to represent the depth of penetration of each AEM sounding, and assigned a level of uncertainty to each value. We may then expect that the shallowest region of the density and magnetization models should assimilate some of the characteristics of the AEM resistivity model. Similarly, we expect that the AEM resistivity model should be enhanced by the structures shown in the density and magnetization models at depth.

As in our previous experiments, we also used the data shown Figure 2a, started from homogeneous models and tested several smoothness parameters. Notably, the resulting AEM constrained models of this experiment (Figure 4) acquired several structures that were not present in any of the previous experiments. Figures 4a and 4b show that, despite their limited depth of investigation, the AEM data eliminated unrealistic shallow annular features present in the magnetic and gravity models of the previous experiments. Correspondingly, the lateral-stitching artifact of the original AEM model was removed and fully decoupled from the deeper and larger structures resolved mainly by the gravity and magnetic data. It is remarkable that, despite the increased smoothness, the AEM data residuals associated to this model decreased in one order of magnitude (cf. Figures 2f and 4d). This accounts for the irrelevance of the sharp layering commonly sought in 1D AEM inversions (e.g. Figure 2e).

GEOSPECTRAL IMAGE COMPARISONS

Although model interpretation can be made from the individual models, we preferred an integrated interpretation of the corresponding geospectral images and signatures (Gallardo, 2007). For this, we assigned a specific RGB-colour band to each physical property. For potential future comparisons, we adopted the color convention of Gallardo and Thebaud (2012) and assigned Red for density contrast, Green to magnetization contrast and the remaining Blue band to logarithmic electrical resistivity. The resulting geospectral images are shown in Figure 5 and their corresponding geospectral signatures are shown in Figure 6 (second experiment) and 7 (third experiment). From the comparison of the geospectral images of Figure 5, we may note that the major structures are clearly driven by the gravity and magnetic data. Nevertheless, smaller scale structures are only present in Figure 5b, particularly in the first 500 m below the surface, indicating they are further supported by the AEM data. We must also point out that the persistence of the structure-rich zone located between the 4 km and 8 km profile positions furnishes more solid evidence of a potential collision zone between the two major structures along the profile.

While the geospectral images are useful to identify characteristic subsurface structures, a more detailed lithological consistency analysis is more easily performed in the associated geospectral signatures (Figures 6 and 7). In these plots, specific property cluster can be associated to lithological units whereas cluster-to-clsuter trends can either reflect model smearing (smoothness) or petrophysics. In the first case, the trend requires spatial neighborhood and thus coincidence to zone boundaries. The clearest example is the transition between clusters A and B in Figure 7. We interpret this transition as the division between the shallow structures and the deeper (and larger) structures. This transition occurs approximately at 500 m depth (just bellow the depth of penetration of AEM field data) since we can identify all the colours between these two clusters below the 500 meters mark in the geospectral image and the rest above.

Although the major structures are all well detected, it is difficult to conclude whether the heterogeneity in shallower structures is also needed by the potential field data or just permitted by them. In this last scenario, we may expect the occurrence of pervasive artifacts induced by the layered inversion and stitching of the AEM data. A complete solution to this dilemma has to wait until the actual AEM data are assimilated in the joint inversion.

CONCLUSIONS

Results from this work demonstrate that it is currently possible to assimilate the AEM resistivity structure in gravity and magnetic model in a cross-gradient joint inversion formulation. They also show that potential field data consistently propose larger structures (either at the near surface or at depth), however they are more meaningfully shaped when shallow deemed AEM information is included. Smoothed transitions, in particular, were significantly reduced. We also note that potential field data capability of discriminating preexisting AEM artifacts is limited, but may still favor the lateral continuity of shallower structures common in gathers of one dimensional AEM resistivity models. We acknowledge that better resolution of small scale artifacts still relies on the assimilation of actual AEM data in joint inversion strategies in multidimensional models.

ACKNOWLEDGMENTS

We thank the Geophysical Archive Data Delivery System (GADDS) for the availability of the gravity and magnetic data used in this work. Part of this research was undertaken on the NCI National Facility in Canberra, Australia, which is supported by the Australian Commonwealth Government. Part of the work presented here is supported by the Discovery Program within CSIRO's Minerals Resources and the Science and Industry Endowment Fund (SIEF). We particularly acknowledge Geoscience Australia, for allowing us the use of the GA-LEI inversion code.

REFERENCES

Brodie, R. C., 2010. Holistic Inversion of Airborne Electromagnetic Data: Phd Thesis, The Australian National University.

Doetsch, J., Linde, N., Coscia, I., Greenhalgh, S. A. & Green, A. G., 2010. Zonation for 3D aquifer characterization based on joint inversions of multimethod crosshole geophysical data: Geophysics, 75(6), G53–G64.

Gallardo, L. A., 2007. Multiple cross-gradient joint inversion for geospectral imaging: Geophysical Research Letters, 34(19), 1–5.

Gallardo, L. A. & Meju, M. A., 2003. Characterization of heterogeneous near-surface materials by joint 2D inversion of dc resistivity and seismic data: Geophysical Research Letters, 30(13), 1–3.

Gallardo, L. A. & Meju, M. A., 2004. Joint two-dimensional DC resistivity and seismic travel time inversion with cross-gradients constraints: Journal of Geophysical Research, 109(B03311), 1–11.

Gallardo, L. A. & Meju, M. A., 2007. Joint two-dimensional cross-gradient imaging of magnetotelluric and seismic traveltime data for structural and lithological classification, Geophysical Journal International, 169, 1261–1272.

Gallardo, L. A. & Meju, M. A., 2011. Structure–coupled multiphysics imaging in geophysical sciences: Reviews of Geophysics, 49, 1–19.

Gallardo, L. A., Fontes, S. L., Meju, M. A., Buonora, M. P. & de Lugao, P. P., 2012. Robust geophysical integration through structure-coupled joint inversion and multispectral fusion of seismic reflection, magnetotelluric, magnetic, and gravity images: Example from Santos Basin, offshore Brazil: Geophysics, 77(5), B237–B251.

Gallardo, L. A., and N. Thebaud (2012). New insights into Archean granite-greenstone architecture through joint gravity and magnetic inversion: Geology, 40(3), 215-218.

Lane, R., Green, A., Golding, C., Owers, M., Pik, P., Plunkett, C., Sattel, D., Thorn, B., 2000. An example of 3D conductivity mapping using the TEMPEST airborne electromagnetic system: Exploration Geophysics, 31(2), 162–172.

León-Sánchez, A. M., Gallardo, L. A., Ley-Cooper, A. Y., 2016. Two dimensional cross-gradient joint inversion of gravity and magnetic data sets constrained by airborne electromagnetic resistivity: Submitted to Geophysical Journal International.

Moorkamp, M., Heincke, B., Jegen, M., Roberts, A. W., Hobbs, R. W., 2011. A framework for 3-D joint inversion of MT, gravity and seismic refraction data: Geophysical Journal International, 184, 477–493.

Reeves, C. V., Reford, S. W. & Milligan, P. R., 1997. Airborne Geophysics: Old Methods, New Images, Proceedings of Exploration 97: Fourth Decennial International Conference on Mineral Exploration, 1997, 13–30.

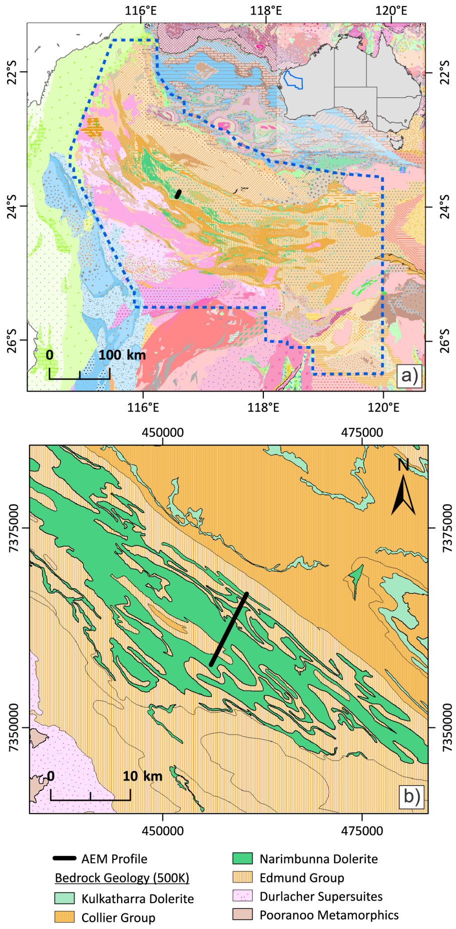

Figure 1. Study area. a) Regional geology and AEM survey limits. b) Local geology and 10 km geophysical profile. Modified from León-Sánchez *et al.* (2016).

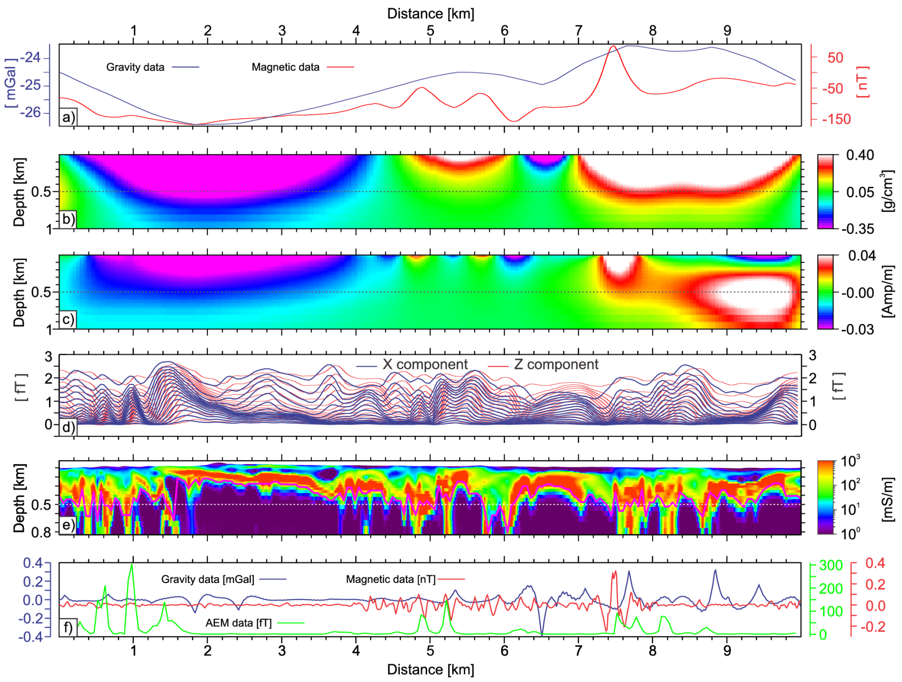

Figure 2. a) Bouguer and RTP profiles. b) Density model obtained after the individual Inversion of Bouguer profile. c) Magnetization model obtained after de individual inversion of RTP profile. d) X and Z components of the AEM survey. e) Stitched 1D AEM inversion model. f) Gravity, RTP, AEM residuals for the individual inversions. Modified from León-Sánchez *et al.* (2016).

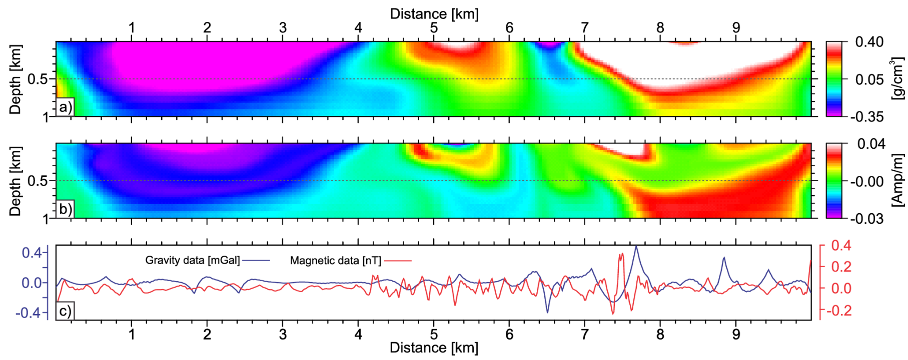

Figure 3. Cross-gradient inversion models. a) Density model. b) Magnetization model. c) Residuals. Modified from León-Sánchez *et al.* (2016).

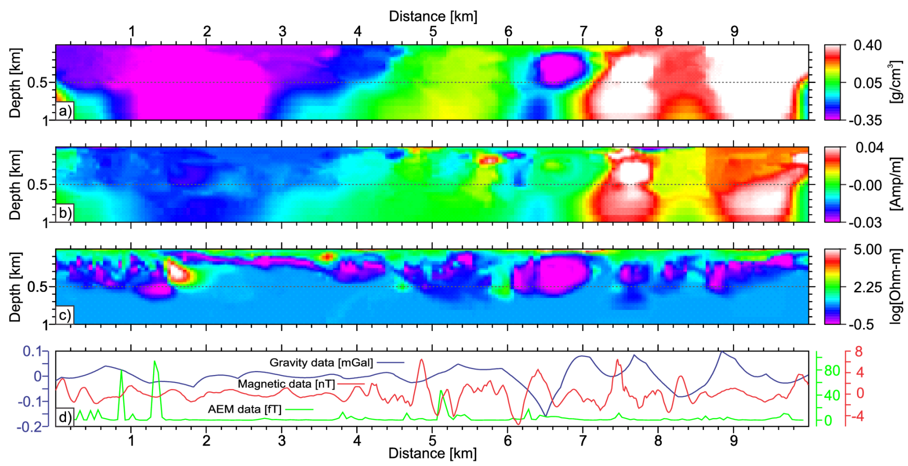

Figure 4. Cross-gradient joint inversion models constrained by AEM resistivity. a) Desnsity model. b) Magnetization model. c) Resistivity model. d) Residuals. Modified from León-Sánchez *et al.* (2016).

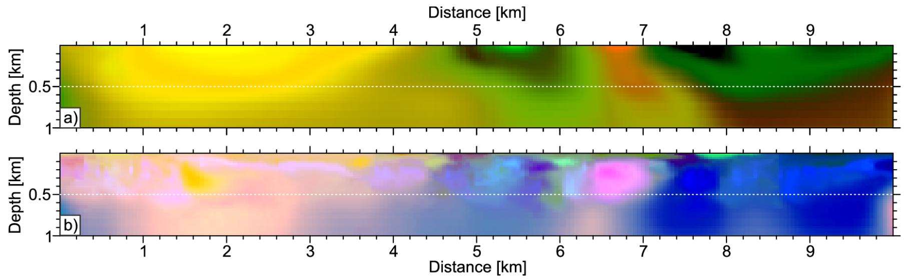

Figure 5. Geospectral images obtained from the cross-gradient joint inversion. a) Only gravity and magnetic data. b) Gravity, magnetic and AEM data. Modified from León-Sánchez *et al.* (2016).

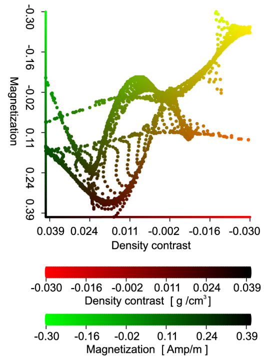

Figure 6. Geospectral signature for Figure 5a. Modified from León-Sánchez *et al.* (2016).

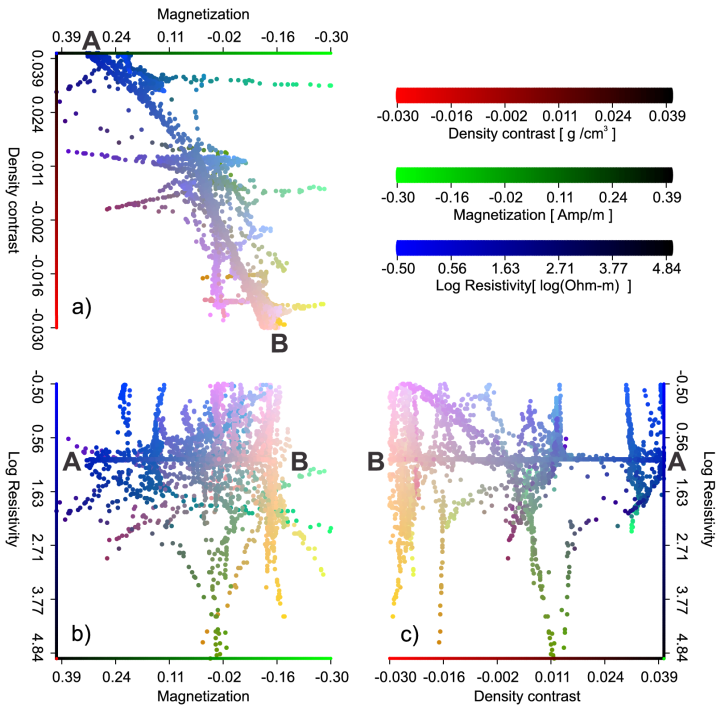

Figure 7. Geospectral signature for Figure 5b. Modified from León-Sánchez *et al.* (2016).